9-8-2014

Mid-IR Hyperspectral Imaging of Laminar Flames for 2-D Scalar Values

Michael R. Rhoby

David L. Blunck
Oregon State University

Kevin C. Gross
Air Force Institute of Technology

Recommended Citation

Michael R. Rhoby, David L. Blunck, and Kevin C. Gross, "Mid-IR hyperspectral imaging of laminar flames for 2-D scalar values," Opt. Express 22, 21600-21617 (2014). https://doi.org/10.1364/OE.22.021600

Mid-IR hyperspectral imaging of laminar flames for 2-D scalar values

Michael R. Rhoby,[1,2] **David L. Blunck**,[3,4] **and Kevin C. Gross**[1,*]

[1]*Department of Engineering Physics, Air Force Institute of Technology, WPAFB, Ohio, USA*
[2] *AFIT PhD student affiliated with the Southwestern Ohio Council for Higher Education, USA*
[3]*Air Force Research Laboratory, Aerospace Systems Directorate, WPAFB, Ohio, USA*
[4]*Now an Assistant Professor of Mechanical Engineering at Oregon State University, Corvallis, Oregon, USA*

[*]*kevin.gross@afit.edu*

Abstract: This work presents a new emission-based measurement which permits quantification of two-dimensional scalar distributions in laminar flames. A Michelson-based Fourier-transform spectrometer coupled to a mid-infrared camera (1.5 µm to 5.5 µm) obtained 256×128 pixel hyperspectral flame images at high spectral ($\delta\tilde{\nu} = 0.75\,\mathrm{cm}^{-1}$) and spatial (0.52 mm) resolutions. The measurements revealed line and band emission from H_2O, CO_2, and CO. Measurements were collected from a well-characterized partially-premixed ethylene (C_2H_4) flame produced on a Hencken burner at equivalence ratios, Φ, of 0.8, 0.9, 1.1, and 1.3. After describing the instrument and novel calibration methodology, analysis of the flames is presented. A single-layer, line-by-line radiative transfer model is used to retrieve path-averaged temperature, H_2O, CO_2 and CO column densities from emission spectra between 2.3 µm to 5.1 µm. The radiative transfer model uses line intensities from the latest HITEMP and CDSD-4000 spectroscopic databases. For the $\Phi = 1.1$ flame, the spectrally estimated temperature for a single pixel 10 mm above burner center was $T = (2318 \pm 19)\,\mathrm{K}$, and agrees favorably with recently reported laser absorption measurements, $T = (2348 \pm 115)\,\mathrm{K}$, and a NASA CEA equilibrium calculation, $T = 2389\,\mathrm{K}$. Near the base of the flame, absolute concentrations can be estimated, and H_2O, CO_2, and CO concentrations of $(12.5 \pm 1.7)\,\%$, $(10.1 \pm 1.0)\,\%$, and $(3.8 \pm 0.3)\,\%$, respectively, compared favorably with the corresponding CEA values of 12.8%, 9.9% and 4.1%. Spectrally-estimated temperatures and concentrations at the other equivalence ratios were in similar agreement with measurements and equilibrium calculations. 2-D temperature and species column density maps underscore the Φ-dependent chemical composition of the flames. The reported uncertainties are 95% confidence intervals and include both statistical fit errors and the propagation of systematic calibration errors using a Monte Carlo approach. Systematic errors could warrant a factor of two increase in reported uncertainties. This work helps to establish IFTS as a valuable combustion diagnostic tool.

OCIS codes: (120.1740) Combustion diagnostics; (280.2470) Flames; (110.4234) Multispectral and hyperspectral imaging; (110.3080) Infrared imaging; (300.2140) Emission; (300.6300) Spectroscopy, Fourier transforms.

#216591 - $15.00 USD Received 9 Jul 2014; revised 15 Aug 2014; accepted 15 Aug 2014; published 29 Aug 2014

References and links

1. K. Kohse-Hoinghaus, J. B. Jeffries (Eds.), *Applied Combustion Diagnostics* (Taylor and Francis, 2002).
2. P. E. Best, P. L. Chien, R. M. Carangelo, P. R. Solomon, M. Danchak, and I. Ilovici, "Tomographic reconstruction of FT-IR emission and transmission spectra in a sooting laminar diffusion flame: species concentrations and temperatures," Combust. Flame **85**, 309–318 (1991).
3. P. R. Solomon, P. E. Best, R. M. Carangelo, J. R. Markham, and P.-L. Chien, "FT-IR emission/transmission spectroscopy for *in situ* combustion diagnostics," Proc. Combust. Instit. **21**, 1763–1771 (1988).
4. D. Blunck, S. Basu, Y. Zheng, V. Katta, and J. Gore, "Simultaneous water vapor concentration and temperature measurements in unsteady hydrogen flames," Proc. Combust. Instit. **32**, 2527–2534 (2009).
5. B. A. Rankin, D. L. Blunck, and J. P. Gore, "Infrared imaging and spatiotemporal radiation properties of a turbulent nonpremixed jet flame and plume," J. Heat Transfer **135**(2), paper 021201 (2013).
6. K. Biswas, Y. Zheng, C. H. Kim, and J. Gore, "Stochastic time series analysis of pulsating buoyant pool fires," Proc. Combust. Instit. **31**, 2581–2588 (2007).
7. L. Ma, W. Cai, A. W. Caswell, T. Kraetschmer, S. T. Sanders, S. Roy, and J. R. Gord, "Tomographic imaging of temperature and chemical species based on hyperspectral absorption spectroscopy," Opt. Express **17**(10), 8602–8613 (2009).
8. K. C. Gross, K. C. Bradley, and G. P. Perram, "Remote identification and quantification of industrial smokestack effluents via imaging Fourier-transform spectroscopy," Environ. Sci. Technol. **44**, 9390–9397 (2010).
9. J. L. Harley, B. A. Rankin, D. L. Blunck, J. P. Gore, and K. C. Gross, "Imaging Fourier-transform spectrometer measurements of a turbulent nonpremixed jet flame," Opt. Lett. **39**(8), 2350–2353 (2014).
10. R. I. Acosta, K. C. Gross, G. P. Perram, S. Johnson, L. Dao, D. Medina, R. Roybal, and P. Black, "Gas phase plume from laser irradiated fiberglass reinforced polymers via imaging Fourier-transform spectroscopy," Appl. Spectrosc. **68**(7), 723–732 (2014).
11. M. S. Wooldridge, P. V. Torek, M. T. Donovan, D. L. Hall, T. A. Miller, T. R. Palmer, M. S. Wooldridge, P. V. Torek, M. T. Donovan, D. L. Hall, T. A. Miller, T. R. Palmer, and C. R. Schrock, "An experimental investigation of gas-phase combustion synthesis of SiO_2 nanoparticles using a multi-element diffusion flame burner," Combust. Flame **131**, 98–109 (2002).
12. T. R. Meyer, S. Roy, T. N. Anderson, J. D. Miller, V. R. Katta, R. P. Lucht, and J. R. Gord, "Measurements of OH mole fraction and temperature up to 20 kHz by using a diode-laser based UV absorption sensor," App. Opt. **44**, 6729–6740 (2005).
13. K. C. Gross, P. Tremblay, K. C. Bradley, M. Chamberland, V. Farley, and G. P. Perram, "Instrument calibration and lineshape modeling for ultraspectral imagery measurements of industrial smokestack emissions," Proc. SPIE **7695**, paper 769516 (2010).
14. V. Farley, A. Vallières, M. Chamberland, A. Villemaire, and J. F. Legault, "Performance of the FIRST, a longwave infrared hyperspectral imaging sensor," Proc. SPIE **6398**, 6398T (2006).
15. H. E. Revercomb, H. Buijs, H. B. Howell, D. D. Laporte, W. L. Smith, and L. A. Sromovsky, "Radiometric calibration of IR Fourier transform spectrometers: solution to a problem with the high-resolution interferometer sounder," App. Opt. **27**, 3210–3218 (1988).
16. P. Tremblay, K. C. Gross, V. Farley, M. Chamberland, A. Villemaire, G. P. Perram, "Understanding and overcoming scene-change artifacts in imaging Fourier-transform spectroscopy of turbulent jet engine exhaust," Proc. SPIE **7457**, paper 74570F (2009).
17. L. Mertz, *Transformations in Optics* (Wiley-Interscience, 1965).
18. D. B. Chase, "Phase correction in FT-IR," Appl. Spectrosc. **36**(3), 240–244 (1982).
19. S. P. Davis, M. C. Abrams, and J. W. Brault, *Fourier Transform Spectrometry* (Academic Press, 2001).
20. L. S. Rothman, I. E. Gordon, R. J. Barber, H. Dothe, R. R. Gamache, A. Goldman, V. I. Perevalov, S. A. Tashkun, and J. Tennyson, "HITEMP, the high-temperature molecular spectroscopic database," J. Quant. Spectrosc. Radiat. Transfer **111**, 2139–2150 (2010).
21. S. A. Tashkun and V. I. Perevalov, "CDSD-4000: high-resolution, high-temperature carbon dioxide spectroscopic databank," J. Quant. Spectrosc. Radiat. Transfer **112**, 1403–1410 (2011).
22. L. S. Rothman, C. P. Rinsland, A. Goldman, S. T. Massie, D. P. Edwards, J.-M. Flaud, A. Perrin, C. Camy-Peyret, V. Dana, J.-Y. Mandin, J. Schroeder, A. Mccann, R. R. Gamache, R. B. Wattson, K. Yoshino, K. V. Chance, K. W. Jucks, L. R. Brown, V. Nemtchinov, and P. Varanasi, "The HITRAN molecular spectroscopic database and HAWKS (HITRAN atmospheric workstation): 1996 edition," J. Quant. Spectrosc. Radiat. Transfer **60**(5), 665–710 (1998).
23. S. Gordon and B. J. McBride, "Computer program for calculation of complex chemical equilibrium compositions and applications," RP-1311, NASA (1996).
24. S. Depraz, M. Y. Perrin, P. Riviere, and A. Soufiani, "Infrared emission spectroscopy of CO_2 at high temperature. Part I: Experimental setup and source characterization," J. Quant. Spectrosc. Radiat. Transfer **113**, 1–13 (2012).
25. S. Depraz, M. Y. Perrin, P. Riviere, and A. Soufiani, "Infrared emission spectroscopy of CO_2 at high temperature. Part II: Experimental results and comparisons with spectroscopic databases," J. Quant. Spectrosc. Radiat. Transfer **113**, 14–25 (2012).
26. R. I. Acosta, "Imaging Fourier transform spectroscopy of the boundary layer plume from laser irradiated poly-

#216591 - $15.00 USD Received 9 Jul 2014; revised 15 Aug 2014; accepted 15 Aug 2014; published 29 Aug 2014

mers and carbon materials," Ph.D. dissertation, AFIT-ENP-DS-14-J-8, Air Force Institute of Technology (2014).

1. Introduction

Scalar measurements in flames are needed for understanding combustion phenomenon, validating chemical kinetic models, and verifying numerical simulations. Intrusive measurements, such as temperature sensing via thermocouples or gas sampling, are straightforward to implement at discrete locations. Measurements at multiple locations or simultaneous determination of temperature and species (at a location) are more challenging and further disturb the flow field. Laser-based methods provide highly effective, non-intrusive means to interrogate both laminar and turbulent flow fields, and are the cornerstone of combustion diagnostics [1]. These techniques often require sophisticated experimental arrangements with multiple optical access points. Simultaneous measurement of multiple scalar quantities (i.e., temperature and mole fractions of various flame species) typically requires multiple laser sources, and mapping these with high spatial resolution can be arduous.

Flame emission measurements are another class of nonintrusive diagnostics that complement laser-based techniques. Multiple line-of-sight Fourier-transform spectrometer (FTS) measurements, when paired with appropriate tomographic deconvolution algorithms, can be used to simultaneously determine temperature and mole fractions of major flame species [2, 3]. High-speed infrared cameras with various band-pass filters have been used to map spatial and temporal variations in radiant intensity and relate these to the spatial distribution of scalar values [4] and to various measures of turbulence (e.g. integral length and time scales) [5, 6].

A new flame emission technique using an imaging Fourier-transform spectrometer (IFTS) can provide spatially resolved, detailed (e.g. $\delta\tilde{\nu} = 0.25\,\mathrm{cm}^{-1}$) wide-band (e.g. the mid-IR, 1.5 μm to 5.5 μm) spectra in a single measurement. Such highly resolved spectral measurements across the mid-IR can be used to monitor rotation-vibration emissions from fuels, intermediates, and major combustion products. High-resolution spectra are valuable for tomography algorithms (e.g. [7]) since variations in different scalar values (i.e., temperature and species concentrations) produce distinct and nearly unambiguous changes in the observed spectral emissions. Previously, IFTS has been used to identify pollutants and quantify species concentrations in the non-reacting turbulent exhaust plume from a coal-fired power plant smokestack [8]. More recently, IFTS has been employed in the measurement and qualitative assessment of a turbulent jet flame [9] and to study plumes arising from laser-material interactions [10]. Tomography techniques have not yet been adapted to IFTS flame measurements. This is significant because the high-resolution spectra, collected simultaneously at multiple lines-of-sight, have the potential to allow significantly improved accuracy in determining scalar values compared to other infrared emission based techniques.

Considering the value of nonintrusive emission-based measurement techniques, and the potential for using an IFTS to determine multiple scalar values in three-dimensions, this paper lays the groundwork for such efforts through the study and analysis of a laminar flame. More specifically, the objectives of this work are as follows: (1) collect spectral information from a laminar flame produced by a canonical burner; (2) develop a novel calibration technique needed for mid-IR flame measurements; (3) pair the latest high-temperature spectroscopic databases with a line-by-line radiative transfer model to estimate two-dimensional scalar values from the spatially-resolved spectra; (4) apply Monte Carlo techniques to understand systematic calibration errors on spectrally-retrieved scalars; (5) compare scalar estimates to those reported in the literature to assess capabilities and limitations of this new technique. This work is a key step in the development of IFTS for three-dimensional scalar estimation and should serve as a benchmark for future applications of IFTS to the study of reacting flows.

#216591 - $15.00 USD Received 9 Jul 2014; revised 15 Aug 2014; accepted 15 Aug 2014; published 29 Aug 2014

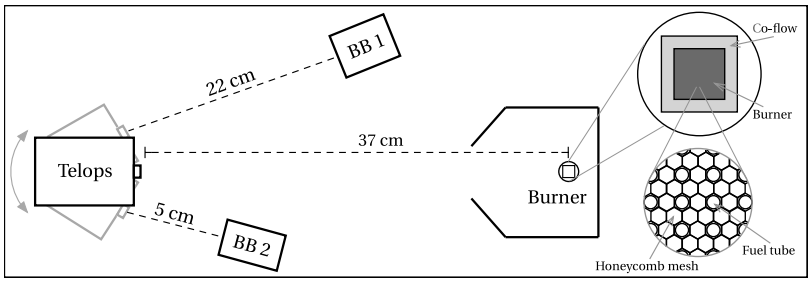

Fig. 1. Schematic of the experimental arrangement. Important relative distances are provided as the image is not to scale. The Telops camera was placed on a rotation platform for fast and accurate transitions between the flame and calibration sources. An expanded view of the burner surface is provided to show the fuel tube and honeycomb mesh arrangement.

2. Experimental

In this work, a well-characterized, partially-premixed ethylene (C_2H_4) flame was studied to allow comparisons with scalar values reported in the literature. The flame was produced by a Hencken burner, which has a 25.4 mm × 25.4 mm square burner with an array of fuel tubes arranged within a honeycomb mesh through which the oxidizer flows. Immediately surrounding this is a similar honeycomb arrangement 6.4 mm wide consisting of tubes which carry an inert co-flow gas (N_2) to improve flame stability. The fuel and oxidizer mix shortly above the burner, resulting in a partially premixed flame. Additional details regarding the burner can be found in the literature [11, 12]. The Hencken burner was placed in a three-sided enclosure to minimize room disturbances. To minimize reflections, the enclosure was coated in a textured diffuse black paint. A schematic of the experimental set-up and detailed view of the Hencken burner is provided in Fig. 1. The flame was produced by flowing 12.21 standard liters per minute (SLPM) of air and 0.69 SLPM to 1.11 SLPM of ethylene (C_2H_4) through the burner. This produced equivalence ratios between 0.8 and 1.3. Temperature and OH mole fractions from a similarly configured Hencken burner were previously measured via laser absorption measurements [12]. 12.0 SLPM of N_2 co-flow was used to minimize entrainment of lab air and matched the conditions reported in the literature. Flow rates were controlled using MKS 1480A ALTA mass flow controllers which have an accuracy of $\pm 1\%$ of the set point flow rate. Laboratory conditions were steady with a temperature of 297 K, pressure of 976 hPa, and an 18.5% relative humidity.

A Telops Hyper-Cam MW-E imaging Fourier-transform spectrometer (IFTS) was used to capture mid-infrared (MWIR, 1.5 µm to 5.5 µm) hyperspectral radiation emitted by the Hencken burner flame. The IFTS features a traditional Michelson interferometer coupled to a high-speed 320×256 Indium Antimonide staring focal-plane array (FPA) via $f/2.5$ imaging optics. The pixel pitch is 30 µm and the optics produce a mean RMS spot size of 14 µm across the array. Instrument details can be found in the literature [9, 13, 14]. An external $0.25\times$ telescope expanded the field-of-view and provided an effective focal length of 21.5 mm. The IFTS was located a distance $d = 373$ mm from the center of the flame with its optical center located approximately $u_0 = 60$ mm above the burner. The spatial resolution of each pixel was 0.52 mm × 0.52 mm at the flame (the image plane). Under the paraxial, thin-lens approximation, the depth of focus is 43 mm. This exceeds the detectable flame width, and due to its symmetry, indicates that each pixel's signal corresponds to photons emitted along the full line-of-sight through the flame. For this experiment, the FPA captured the two-dimensional data with a 40 µs integration time on a 256×128 pixel sub-window. The spectral resolution was set to $\delta\tilde{\nu} = 0.75\,\mathrm{cm}^{-1}$ where $\delta\tilde{\nu}$ is the full-width at half-maximum of the instrument line shape (ILS). Symmetric interferograms were obtained by continuously scanning the Michelson interferometer at a uniform speed

#216591 - $15.00 USD Received 9 Jul 2014; revised 15 Aug 2014; accepted 15 Aug 2014; published 29 Aug 2014

($0.21\,\mathrm{cm\,s^{-1}}$) to a maximum optical path difference (OPD) of $x_m = 0.8\,\mathrm{cm}$, with images captured every 632.8 nm. This corresponds to a *camera frame rate* of 3.4 kHz. Each interferometric "cube" consisting of 25,278 images was acquired in 7.5 s, and corresponds to an *interferometric cube rate* of 0.13 Hz. Each cube requires more than 1.5 GB of storage. To balance the needs of capturing a statistically sufficient sampling of the flame and efficiently storing and processing a large data set, 50 interferometric cubes of each flame were acquired and averaged.

Data for radiometric calibration was collected using 2 in and 6 in square CI Systems blackbody sources placed at distances of 5 cm and 22 cm, respectively, from the camera. This ensured each over-filled the instrument's field-of-view (FOV). A standard [15] two-point calibration—modified for noise suppression (see Sec. 3.2)—was performed to remove both system response and instrument self-emission from the raw signal by measuring the 2 in and 6 in blackbodies at 200 °C and 580 °C, respectively. Correction of the spectral axis due to dispersion in the imaging system was performed as previously described [13]. Temperatures for the 2 in and 6 in are accurate to within $\pm 0.3\%$ and $\pm 1.0\%$, respectively, of the set-point temperatures. Spectral emissivities for the 2 in and 6 in blackbodies are reported to be 0.980 ± 0.004 and 0.96 ± 0.02, respectively. The manufacturer-reported blackbody uncertainties were taken to represent 95% confidence intervals (CIs), and were used to perform a Monte Carlo error analysis of both the calibrated radiances and spectrally-retrieved scalar values. This analysis is presented in a later section. Calibrated radiance spectra $L_i(\tilde{\nu})$ are reported at each pixel (i) with units $\mu\mathrm{W/(cm^2\,sr\,cm^{-1})}$. The spectral variable $\tilde{\nu} = \lambda^{-1}$ is expressed in wavenumbers (reciprocal wavelength, $\mathrm{cm^{-1}}$).

3. Radiation model

3.1. Interferogram formation

Here, great care is taken in describing the modeling, approach, and calibration of data since this work develops a new technique that will serve as a benchmark for future studies. A Michelson imaging interferometer splits the incident radiation into two beams and then recombines them so that an interference pattern is produced at the focal plane array (FPA). The measured signal at each pixel (i) of the FPA, $I_i(x)$, varies with the optical path difference, $x = vt$, as the interferometer scans in time, t, at a constant speed, v. For a *static* scene with a radiance spectrum $L_i(\tilde{\nu})$, the measured signal after passing through an ideal interferometer is given by

$$I_i(x) = \int_0^\infty \left(1 + \cos\left(2\pi\tilde{\nu}x\right)\right) G_i(\tilde{\nu}) \left(L_i(\tilde{\nu}) + L_i^I(\tilde{\nu})\right) \mathrm{d}\tilde{\nu} \tag{1}$$

$$= I_i^{\mathrm{DC}} + I_i^{\mathrm{AC}}(x). \tag{2}$$

$G_i(\tilde{\nu})$ accounts for the spectrally-dependent response of the instrument, and includes factors such as the quantum efficiency of the detector, as well as transmission and reflection losses within the optics. Note that $G_i(\tilde{\nu})$ rapidly approaches 0 as $\tilde{\nu}$ approaches the band-gap of the photodetector material (InSb, $\tilde{\nu}_{\mathrm{b.g.}} \simeq 1855\,\mathrm{cm^{-1}}$). The at-detector radiance is a combination of both the source radiation and the thermally-generated photons within the instrument, $L_i^I(\tilde{\nu})$, and thus requires at least two unique calibration measurements to determine the scene radiance spectra, $L_i(\tilde{\nu})$. The total scene intensity is comprised of a constant offset I_i^{DC} — the unmodulated, spectrally-integrated signal — and a modulated component, $I_i^{\mathrm{AC}}(x)$, which encodes the spectral information via the cosine transform. The raw spectrum is obtained by Fourier-transformation of the AC term, and application of standard calibration techniques [15] produces $L_i(\tilde{\nu})$. An important modification to the standard calibration approach is required for high-temperature flames and is described in the next section.

In the present work, the flame becomes unsteady about 20 mm above the burner due to buoyancy effects. This caused substantial, systematic variation in scene radiance so that $L_i = L_i(\tilde{\nu}, t)$

#216591 - $15.00 USD Received 9 Jul 2014; revised 15 Aug 2014; accepted 15 Aug 2014; published 29 Aug 2014

with a fluctuation timescale much shorter than the interferometric measurement time scale. The DC term is no longer a constant, but captures the broadband radiance fluctuations caused by buoyancy effects in the flame. Furthermore, the AC term is no longer the cosine transform of a static spectrum, and its Fourier-transformation is difficult to interpret quantitatively. If the dynamic source is ergodic and a statistically sufficient number of data cubes are acquired, then the mean interferogram corresponds to the mean source radiance. The Fourier-transform is a linear transform mapping the interferogram to the spectrum and thereby preserves this association. However, the radiance spectrum is a nonlinear function of the flame scalar values, so interpretation of the flame radiance must be performed carefully.

There is significant information content about the unsteady fluctuations encoded in a single interferogram. To appreciate this, note that the Michelson encodes spectral information by modulating the intensity at frequencies above $f_{\text{b.g.}} = v\,\tilde{\nu}_{\text{b.g.}}$. In these measurements, the mirror velocity was $v = 0.21\,\text{cm}\,\text{s}^{-1}$ yielding $f_{\text{b.g.}} \simeq 390\,\text{Hz}$. Thus, at frequencies below $f_{\text{b.g.}}$, the intensity fluctuations can be attributed to radiance fluctuations. Application of an appropriate low-pass filter removes the intensity modulations caused by the action of the Michelson, thereby yielding a high-speed infrared intensity images (i.e., a movie) of the unsteady flow. This will facilitate interpretation of the spectra presented in this work, and more generally enables flow field analysis similar to what is currently performed by infrared cameras [4, 5]. It is also possible to take advantage of the DC fluctuations and produce "quantile interferograms" which map to spectra associated with the flame at various integrated intensity quantiles [16]. We plan to adapt this approach to the study of this and other unsteady flames in a follow-on effort.

3.2. Instrument calibration

Radiometric calibration of FTS is well established for low temperature participating media [8, 13, 15]. However, high flame temperatures required the development of a new calibration approach. We first review the standard FTS calibration methodology, which starts by assuming the instrument responds linearly to incident radiation. Observation of a blackbody source at two distinct temperatures affords the pixel-wise (i) determination of the system response ($G_i(\tilde{\nu})$, gain) and self-emission ($L_i^I(\tilde{\nu})$, offset) which define the linear transform mapping scene radiance $L_i(\tilde{\nu})$ to instrument response $Y_i(\tilde{\nu})$:

$$Y_i(\tilde{\nu}) = G_i(\tilde{\nu})\left(L_i(\tilde{\nu}) + L_i^I(\tilde{\nu})\right). \tag{3}$$

Since $Y_i(\tilde{\nu})$ is in general a complex quantity, complex calibration coefficients are determined, thereby ensuring the signal is contained in the real part and noise is equitably distributed among both the real and imaginary parts.

This calibration approach has practical limitations for this work. The flame of interest has a nominal temperature of ~2400 K and exhibits strong, selective emission between $2100\,\text{cm}^{-1}$ to $2400\,\text{cm}^{-1}$ and between $3100\,\text{cm}^{-1}$ to $4200\,\text{cm}^{-1}$. Elsewhere, the flame emission is negligible, and the integrated radiance across the IFTS's bandpass produces a signal comparable to that produced by a 550 °C blackbody. Thus, to ensure the flame integrated radiance is bracketed by the calibration integrated radiances, the higher-temperature blackbody should exceed this temperature. However, the integrated radiance corresponding to this blackbody temperature is constrained by the upper limit of the camera's dynamic range. In the present work, a wide-area blackbody set to 580 °C was used, and filled ~90% of the FPA dynamic range at the zero path difference (ZPD, $x = 0$). For comparison, the brightest part of the flame used ~85% of the dynamic range at ZPD. Between $3250\,\text{cm}^{-1}$ and $4250\,\text{cm}^{-1}$, the signal-to-noise ratio (SNR) of a typical flame measurement can exceeded the SNR of the high-temperature blackbody by a factor of three. The blackbody curve at this temperature monotonically decreases with $\tilde{\nu}$ across the IFTS bandpass. Moreover, the number of photons per unit energy emitted by the blackbody

#216591 - $15.00 USD Received 9 Jul 2014; revised 15 Aug 2014; accepted 15 Aug 2014; published 29 Aug 2014

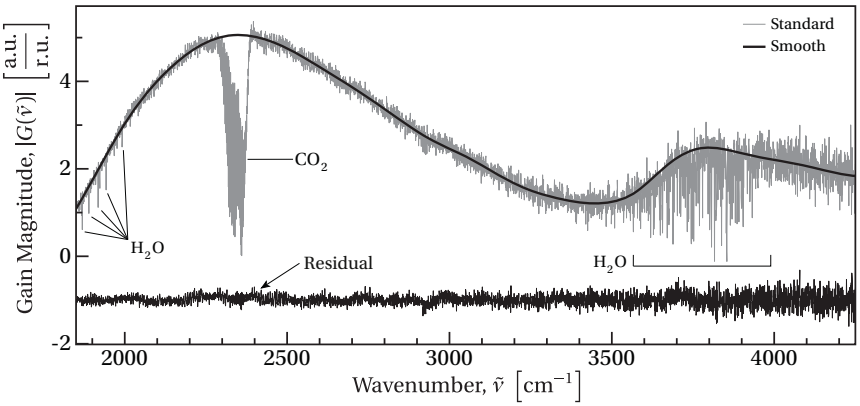

Fig. 2. Representative single-pixel gain curve magnitude computed from standard calibration method (grey) compared with the gain curve magnitude obtained after atmospheric correction and spline smoothing (black). Residual difference between standard gain curve and the product of the smooth gain curve with atmospheric transmittance function is provided, offset by $-1\,^{\text{a.u.}}/_{\text{r.u.}}$. Atmospheric absorption features are annotated. Here, a.u. represents arbitrary units and r.u. represents radiometric units.

decreases as $1/\tilde{\nu}$ across the detector bandpass. These effects reasonably limit the achievable SNR of the gain term at higher wavenumbers. Since the calibrated scene radiance is obtained via division by $G_i(\tilde{\nu})$, a low-SNR gain can introduce errors in $L_i(\tilde{\nu})$ that are non-normally distributed, complicating quantitative interpretation of flame spectra.

The InSb quantum efficiency, optics transmittances, and other factors affecting system response are such that the gain magnitude, $|G_i(\tilde{\nu})|$, exhibits a smooth, slow variation with $\tilde{\nu}$. A possible exception to this is the effect that the atmospheric transmittance profile would have on $|G_i(\tilde{\nu})|$, if it is not accounted for when modeling the at-sensor radiance from a distant blackbody source. Our calibration methodology accounts for atmospheric absorption, and leverages the expectation of smoothness of the resulting gain term. First, Mertz phase correction [17, 18] is performed when converting calibration (and flame) interferograms to raw spectra. Then a least-squares smoothing spline is applied to each pixel's gain magnitude and the gain phase is set to zero. (Phase correction ensured the gain phase was zero-mean noise.) It was determined via graphical inspection that fifteen spline points adequately captured the variation in $|G_i(\tilde{\nu})|$ without fitting to the noise. The imaginary component of the calibrated flame radiance is not discarded as it can be used to assess calibration quality and estimate SNR.

Single-pixel gain curves obtained via the standard calibration method and our modified approach are compared in Fig. 2. The gain determined from the standard calibration without atmospheric compensation is shown in grey. Overlaid with this curve is the modified gain obtained using atmospheric compensation and a spline fit. The residual difference between the standard gain and the smooth gain, multiplied by the atmospheric transmittance profile, is also shown. The largely unstructured residuals are dominated by noise, indicating the effectiveness of the atmospheric compensation and spline smoothing.

3.3. Spectral radiation model for determining scalar values

A simple model describing the apparent line-of-sight flame radiance was used to estimate temperature and relative species concentrations from the measured spectra. The spectral radiance $L_i(\tilde{\nu})$ from a non-scattering source in local thermodynamic equilibrium (LTE) can be approxi-

#216591 - $15.00 USD Received 9 Jul 2014; revised 15 Aug 2014; accepted 15 Aug 2014; published 29 Aug 2014

mated by

$$L_i(\tilde{\nu}) = \tau(\tilde{\nu})\,\varepsilon(\tilde{\nu},T,\vec{\xi})\,B(\tilde{\nu},T) * \mathrm{ILS}(\tilde{\nu}) \tag{4}$$

where $\varepsilon(\tilde{\nu},T,\vec{\xi})$ is the gas emissivity, which is a function of gas mole fractions $\vec{\xi}$, and $B(\tilde{\nu},T)$ is Planck's blackbody radiance distribution at temperature T. Here, $\tau(\tilde{\nu})$ represents the transmittance of the atmosphere between the flame and instrument. Measured meteorological conditions were used to estimate $\tau(\tilde{\nu})$. $\mathrm{ILS}(\tilde{\nu})$ represents the instrument line shape of a Fourier-transform spectrometer with which the "monochromatic" flame spectrum is convolved. No apodization of the interferograms was performed, thus $\mathrm{ILS}(\tilde{\nu}) = 2\pi x_m \mathrm{sinc}(2\pi x_m \tilde{\nu})$ [13, 19]. In a non-scattering medium, the spectral emissivity is related to the scalar values via

$$\varepsilon(\tilde{\nu},T,\vec{\xi}) = 1 - \exp\left(-lN\sum_i \xi_i \sigma_i(\tilde{\nu},T)\right) = 1 - \exp\left(-\frac{l}{l_{\mathrm{MFP}}}\right) \tag{5}$$

where the number density $N = P/(k_B T)$, l is the path length through the flame, ξ_i is the i^{th} species mole fraction, and $\sigma_i(\tilde{\nu},T)$ is its corresponding absorption cross-section. The product $\vec{q} = \vec{\xi} l$ is denoted the fractional column density. The reciprocal of the number density and sum over mole-fraction weighted cross-sections defines the photon mean-free-path, l_{MFP}, in the model flame.

The phenomenological absorption cross-section σ_i for the i^{th} species represents a sum over discrete spectral emission lines, each with its own line intensity, S_{ij}, and line shape, $\phi_{ij}(\tilde{\nu})$, via:

$$\sigma_i(\tilde{\nu},T) = \sum_j S_{ij}(T)\phi_{ij}(\tilde{\nu} - \tilde{\nu}_j, T). \tag{6}$$

The line shape term is dependent on the partial pressures of the various species. In this work, the Voigt profile is used and a constant pressure of $P = 976\,\mathrm{hPa}$ is assumed throughout the flame. In computing the Voigt profile, species are assumed dilute so that only broadening rates for dry air are used. Line mixing and continuum effects on the line shape were not included. Parameters to compute absorption cross-sections for H_2O and CO were computed using the HITEMP spectroscopic database [20], and cross-sections for CO_2 were computed using the CDSD-4000 spectroscopic database [21]. The phenomenological cross section includes the weighting of internal state populations via Boltzmann statistics (assuming LTE), and the temperature dependence is computed (see the appendix in [22]) using the appropriate partition function data accompanying the HITEMP and CDSD-4000 databases. Cross-sections for each species were pre-computed at temperatures between 300 K to 3000 K every 50 K, and quadratic interpolation was used to compute cross-sections at arbitrary temperatures.

Spectral estimates of the flame temperature and fractional column densities were determined at each pixel by fitting Eq. (4) to the corresponding measured spectrum. This was accomplished by minimizing the sum of squared differences between the data and model parameters, T and $\vec{q} = (q_{\mathrm{H_2O}}, q_{\mathrm{CO_2}}, q_{\mathrm{CO}})$, using a Nelder-Mead direct search followed by a Levenberg-Marquardt gradient-based error minimization. Atmospheric H_2O and CO_2 concentrations were also model parameters to ensure the best possible estimate of τ. In the $\Phi = 0.8$ and $\Phi = 0.9$ flames, a small baseline oscillation was observed in spectral regions absent of line emission from the combustion gases. As discussed later, this only occurred in certain flame locations and is likely the result of insufficient temporal averaging over the flame unsteadiness. To mitigate the impact of the baseline oscillation on the spectral fit results, a 4^{th}-order polynomial was added to the model for the $\Phi = 0.8$ and $\Phi = 0.9$ measurements. The spectrum at each pixel contains 3000 unique radiance values, ensuring the six-parameter or eleven-parameter nonlinear model is highly over-determined.

#216591 - $15.00 USD Received 9 Jul 2014; revised 15 Aug 2014; accepted 15 Aug 2014; published 29 Aug 2014

This model makes a few notable simplifications to the actual radiative transfer problem, the most significant being the assumption of flame homogeneity along each pixel's line-of-sight. This is a reasonable approximation near the base of the Hencken burner where—as supported by flame images presented in the next section—the mixing layer is a small fraction of the total line-of-sight. This assumption is also made in the analysis of OH laser absorption measurements of the similarly configured Hencken flame against which the present results will be compared [12]. The width of the mixing layer steadily increases with height above the flame, and the homogeneity approximation above ~20 mm breaks down. As the mixing layer grows, temperature and density gradients become non-negligible and will systematically bias the fit parameters due to the variation in T and ξ_i along the line-of-sight. Given these limitations, this model can only be used to estimate core flame temperature and concentrations near the base of the burner and along lines-of-sight that are not dominated by the mixing layer, i.e., $u < 20\,\text{mm}$ and $|v| < 10\,\text{mm}$. Here u and v represent the flame coordinate system, and are defined in Fig. 3. A multi-layer deconvolution approach can be developed for flames or regions where mixing is significant, as discussed previously. Within this region, absolute concentrations are determined via $\xi_i = q_i/l$ where $l = 25.4\,\text{mm}/\cos(\theta(u))$ and $\theta(u) = \tan^{-1}\left((u_0-u)/d\right)$ is a small angle which accounts for the line-of-sight through the flame for rays a distance $y_0 - y$ from the optical center of the camera. Elsewhere in the flame, the biased estimates, due to mixing, of T and $\vec{q}$ are to be interpreted as path-averaged quantities. Note that they are not true path-averaged quantities due to the nonlinear dependence T and ξ_i have on measured radiance. A multilayer deconvolution method is being developed to estimate 3-D distributions of temperature and concentrations.

Other model simplifications include neglecting the transport of background radiation through the plume and atmospheric path radiance generated between the flame and sensor. However, these quantities are negligible compared to the flame radiance. The impact of ignoring collisional self-broadening in the Voigt profile has not been assessed, however its impact is expected to be small as typical line widths are narrower than the width of ILS($\tilde{\nu}$).

4. Results

4.1. Data overview

Figure 3 compares the broadband imagery captured by the IFTS in a single interferometric measurement at each equivalence ratio. The imagery was obtained by applying a low-pass filter along the OPD dimension with a cut-off frequency below $f_{\text{b.g.}}$. The left half of each image corresponds to the time-averaged intensity in raw camera counts. Near the base of each burner, the intensity rapidly increases with height, peaking at about 10 mm, and then decaying more gradually with increasing distance from the burner. The most fuel lean trial with $\Phi = 0.8$ exhibits the swiftest decay in intensity with height and the fuel rich trial with $\Phi = 1.1$ shows the slowest intensity decay with height. Traversing each flame axially, the transition from flame emissions to background occurs near $v = \pm 13\,\text{mm}$ near the base of the burner. This mixing layer remains small up to about $u = 10\,\text{mm}$. Due to the symmetry of the burner, it follows that the mixing layer represents a small contribution to the measured line-of-sight radiance near the burner. The mixing layer increases in size with additional height above the burner due to entrainment of the N_2 co-flow.

The right half of each image shows the intensity coefficient of variation (CoV), which is the standard deviation of intensity normalized by the mean intensity. Near the base of the burner, each flame is steady, yielding intensity values on the order of 25,000 to 30,000 counts with minimal variations (CoV $< 2\%$). Around 20 mm above the burner, buoyancy effects produce unsteady flow, causing intensity variations which increase with height and are more than 15% of the mean intensity by 40 mm. Unsteady intensity fluctuations were largest for the $\Phi = 0.9$ trial with CoV values exceeding 22% in the mixing layer near 60 mm above the burner. Interestingly,

#216591 - $15.00 USD Received 9 Jul 2014; revised 15 Aug 2014; accepted 15 Aug 2014; published 29 Aug 2014

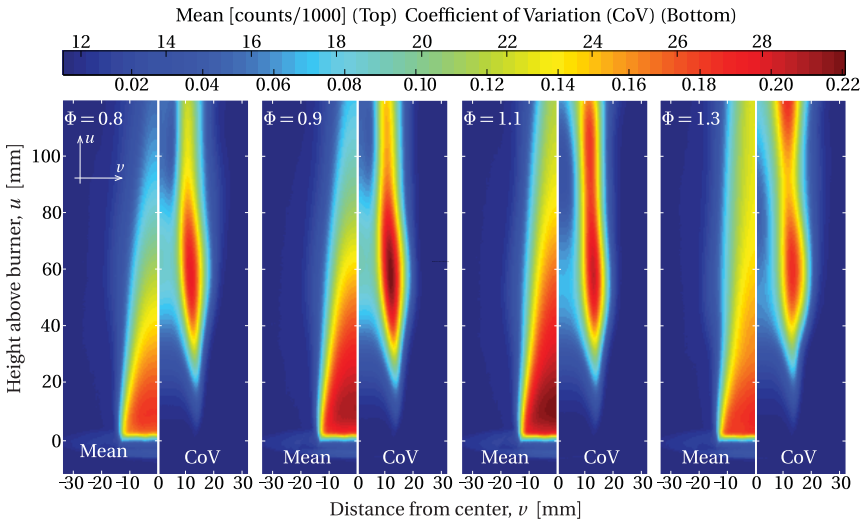

Fig. 3. Split imagery of the symmetric flame for each of the four Φ values tested. Mean camera intensity values are on the left and coefficient of variation (CoV) values are on the right. The top and bottom of the color bar correspond to the mean intensity in 1,000's of counts and CoV values, respectively.

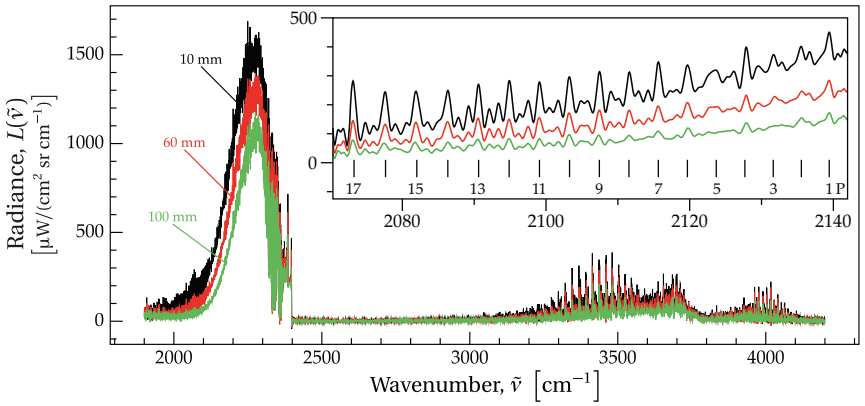

Fig. 4. Three center-flame spectra corresponding to heights 10 mm, 60 mm and 100 mm above the base of the $\Phi = 1.1$ flame. The inset plots presents a detailed view of the P-branch corresponding to the fundamental $1 \rightarrow 0$ emission from CO. Odd numbered rotational levels are marked.

CoV values between 40 mm $\leq u \leq$ 90 mm and $v = 0$ were substantially larger for the fuel lean-flames compared with the fuel-rich flames.

Center-flame spectra at 10 mm, 60 mm and 100 mm above the burner are presented in Fig. 4. The largest emission feature near 2250 cm^{-1} is from the asymmetric stretching mode of CO_2, as well as combination bands at nearly resonant frequencies. Careful inspection of the region between 2000 cm^{-1} to 2150 cm^{-1} reveals the P-branch of CO (see inset plot). The R-branch overlaps with the strong CO_2 emission and becomes difficult to discern. The line emission between 3000 cm^{-1} to 4200 cm^{-1} is primarily due to H_2O rotational fine structure associated with transitions between several vibrational states. Also within this region is weaker broadband emission from CO_2, and very weak spectral emission from OH. The spectral radiance decreases

#216591 - $15.00 USD Received 9 Jul 2014; revised 15 Aug 2014; accepted 15 Aug 2014; published 29 Aug 2014

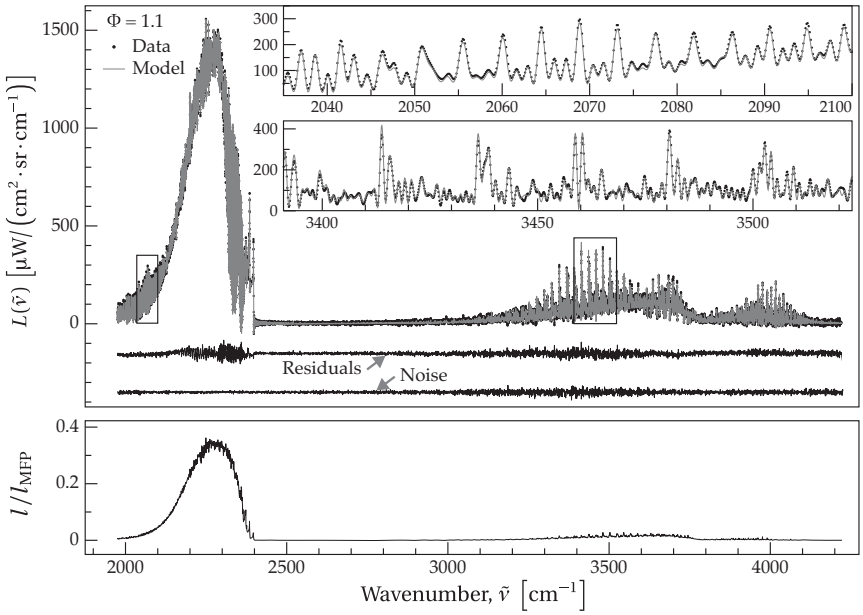

Fig. 5. *Top*: Ethylene $\Phi = 1.1$ center-flame spectrum 10 mm above burner (· black) is compared with a model fit (– gray). Fit residuals, offset by $-150\,\mu W/(cm^2\,sr\,cm^{-1})$, and instrument noise level, offset by $-350\,\mu W/(cm^2\,sr\,cm^{-1})$, are provided. *Bottom*: Ratio of the flame path length, l, to the calculated mean free path of a photon, l_{MFP}, under the conditions estimated by the model fit.

with height due to cooling brought on by mixing with the N_2 co-flow and surrounding air. The entrainment of air enables oxidation of CO to occur with increasing distance from the burner, and by 100 mm CO emission lines are substantially diminished.

4.2. 2-D spectral estimates of scalar values

4.2.1. Single pixel results

Fitting Eq. (4) enables simultaneous retrieval of T and mole fractions ξ_{H_2O}, ξ_{CO_2} and ξ_{CO}. In the top panel of Fig. 5, the emission spectrum between 1975 cm^{-1} to 4225 cm^{-1} is shown for a single pixel at location $(u,v) = (10\,\text{mm}, 0\,\text{mm})$ for the $\Phi = 1.1$ trial. Also provided is the model prediction corresponding to the best-fit parameters of $T = (2318 \pm 19)$ K, $\xi_{H_2O} = (12.5 \pm 1.7)\,\%$, $\xi_{CO_2} = (10.1 \pm 1.0)\,\%$ and $\xi_{CO} = (3.8 \pm 0.3)\,\%$. The measured temperature compares favorably with recent laser diagnostics results [12], (2348 ± 115) K, as well as with NASA CEA [23] equilibrium flame temperature of 2389 K. H_2O, CO_2 and CO mole fractions are in good agreement with the CEA equilibrium values of 12.8%, 9.9% and 4.1% respectively. We are not aware of other experimental determinations of these same species mole fractions for a similarly configured Hencken burner to compare against.

Reported fit parameter errors are the 95% CIs due to measurement noise and the propagation of calibration uncertainties. They do not account for systematic errors in the model. Details on the computation of parameter uncertainties is postponed until Sec. 4.3. The difference between the data and model are also presented in Fig. 5, denoted Residuals, and compared with the imaginary part of the spectrum, denoted Noise. The fit residuals are mostly unstructured with a root-mean-square (RMS) value of 10.1 μW/(cm^2 sr cm^{-1}). The RMS value of the fit residuals is only 1.5 times larger than the RMS value of instrument noise, indicating that the model

#216591 - $15.00 USD Received 9 Jul 2014; revised 15 Aug 2014; accepted 15 Aug 2014; published 29 Aug 2014

describes the flame spectrum well overall. However, some systematic errors are present. This is most evident from the observed structure in the residuals between 2150 cm^{-1} to 2400 cm^{-1}. Within this range, the fit residual RMS value is 5.9 times larger than the instrument noise RMS value. However, the noise in this region is small, and the RMS fit residual in this band is only 3.5% of the RMS signal. The quality of this single pixel spectral fit is representative of the fit quality across the hyperspectral image.

Mixing layer effects may contribute to the systematic fitting errors observed between 2150 cm^{-1} to 2400 cm^{-1}. The bottom panel of Fig. 5 shows the ratio of the flame path length, l, and the calculated mean free path of a photon, l_{MFP} (Eq. (5)), under the conditions estimated by the model fit. This ratio is less than 3% across most of the spectrum, but approaches 40% within the strong CO_2 asymmetric-stretch emission band. This suggests that while the plume is optically thin across most of the spectrum, some optical trapping occurs within this CO_2 band. It follows that emission from the mixing layer will have a larger effect within this band in comparison with the optically thin spectral regions. This interpretation is consistent with the observation that fit residual magnitudes relative to the signal increase with height (i.e. mixing layer width). While the homogeneous assumption is adequate across most of the spectrum and yields spectral retrievals in good agreement with experimental and theoretical predictions, the high fidelity measurements may contain information about small mixing layer effects.

A second contributing factor for systematic fit errors may be associated with limitations of the spectroscopic databases used in this work. Recent measurements [24, 25] of high-temperature (2000 K to 5000 K) CO_2 produced via microwave discharge suggests that systematic errors in the spectral radiance between 2100 cm^{-1} to 2450 cm^{-1} can be up to 10–30%. Similarly, in a recent study involving laser irradiation of graphite targets [26], an empirical emissivity correction factor was needed to adequately reproduce the observed spectral emissions from the hot, CO_2-rich plume above the target within this same spectral region. However, in both of these recent experiments, CO_2 temperatures were much larger than the flame temperatures observed in this work and, in some cases, exceeded the useful temperature range of the CDSD-4000 database. Moreover, the radiative transfer models required to accurately describe the data were considerably more complicated than what is needed to model the Hencken burner flame. Thus, while limitations of the spectroscopic databases cannot be ruled out, their effect on the scalar estimates is likely small given both the good fit quality and the excellent agreement between spectrally-retrieved scalar values with Meyer's results and CEA thermodynamic calculations.

Finally, the point-spread function of the instrument causes subtle mixing of spectral emissions from nearby pixels, and our instrument model does not yet account for these effects. As our future efforts will focus on three-dimensional scalar field reconstruction, these small effects will need to be properly modeled. Given the possible systematic errors due to instrumentation, model simplifications, and limitations of high-temperature spectroscopy databases, actual scalar value uncertainties may exceed those presented here by an additional factor of two. Despite this important caveat, the small fit uncertainties exemplify the benefit of a highly-resolved emission spectrum across a wide band pass for temperature estimation. 3000 unique data points between $1975\,cm^{-1} \leq \tilde{\nu} \leq 4225\,cm^{-1}$ sample myriad H_2O, CO_2 and CO emission lines, each representing a transition between pairs of internal energy levels. When local thermodynamic equilibrium prevails, the population of each internal energy level is governed by the same temperature via the Boltzmann distribution.

4.2.2. Radial and axial fit results

Spectrally-estimated scalars were uniform across the flame near the base of the burner. Figure 6 shows the results for the $\Phi = 1.1$ trial at $u = 10$ mm. The mean temperature obtained for all pixels within 5 mm of flame center was $T = 2317$ K with a standard deviation of 2 K.

#216591 - $15.00 USD Received 9 Jul 2014; revised 15 Aug 2014; accepted 15 Aug 2014; published 29 Aug 2014

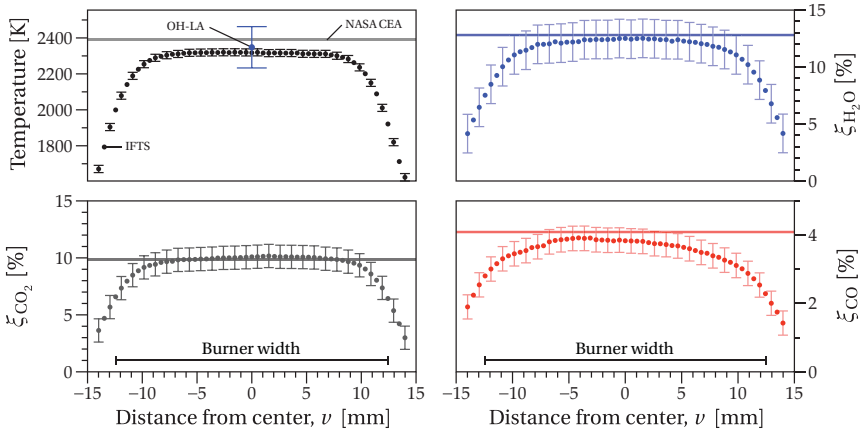

Fig. 6. Spectrally-retrieved scalar values of ethylene flame 10 mm above the burner for the $\Phi = 1.1$ condition. Error bars indicate the 95% confidence interval and only every other bar is shown for clarity. For comparison, the temperature value obtained by OH-laser absorption measurements (•) and NASA CEA values (— ,— ,—) are provided.

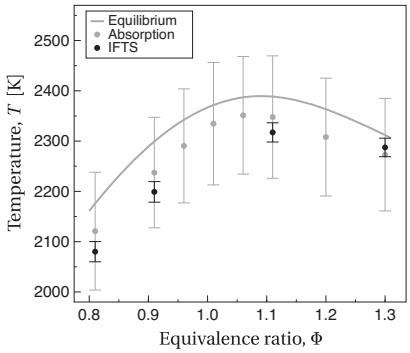

Fig. 7. Variation of spectrally-retrieved average temperature with equivalence ratio in ethylene flame at a height of 10 mm above the burner. Comparison values of temperature measured with OH-laser absorption and chemical equilibrium are from Meyer *et al.* [12].

Note that the pixel-to-pixel temperature variance is approximately ten times smaller than the fit errors associated with the individual spectral estimates (nominally 20 K). For comparison, the corresponding laser-based temperature measurement is also provided. The transition to lines-of-sight dominated by radiance from the mixing layer occurs around ± 10 mm from the center of the burner; beyond this, the retrieved temperature rapidly decays with distance. While the H_2O and CO_2 mole fraction profiles are qualitatively similar in shape to that of temperature, the CO profile is less flat across the center of the flame. Mean values within 5 mm of flame center for H_2O, CO_2, and CO were 12.5% and 10.1%, and 3.8%, respectively. Pixel-to-pixel standard deviations (0.1%, 0.08%, and 0.08%, respectively) were much smaller than measurement uncertainties. The reduction in both temperature and mole fraction in the mixing layer result in SNRs too low to support spectral retrievals beyond $v = \pm 15$ mm.

Temperatures estimated at $u = 10$ mm for each equivalence ratio are compared with the laser absorption measurements [12] and equilibrium calculations in Fig. 7. The results are in very good agreement. IFTS temperature estimates are well within the error bars of the laser-based measurements, and don't differ by more than 30 K. (The error bars provided by Meyer *et al.* are

#216591 - $15.00 USD Received 9 Jul 2014; revised 15 Aug 2014; accepted 15 Aug 2014; published 29 Aug 2014

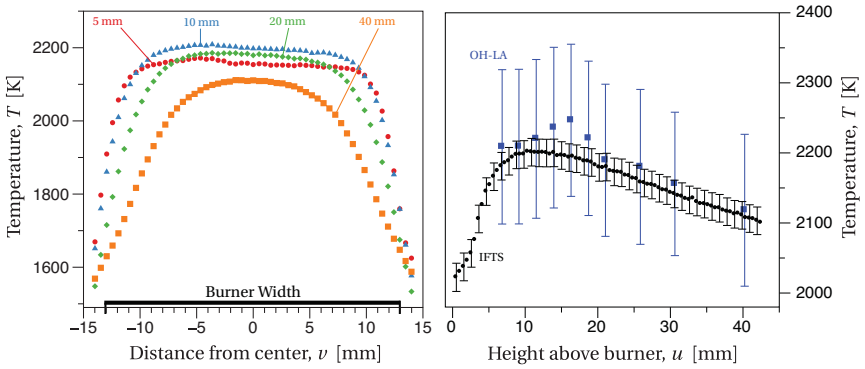

Fig. 8. *Left panel*: Spectrally-retrieved temperature of ethylene flame at heights of 5 mm, 10 mm, 20 mm and 40 mm above the burner for the $\Phi = 0.9$ condition. Error bars are not shown for clarity but have nominal half-widths of approximately 20 K. *Right panel*: Comparison of the spectrally-estimated temperatures (IFTS) with laser absorption measurements (OH-LA) at various heights along the centerline of the $\Phi = 0.9$ flame. Error bars are omitted at every other point for clarity.

not clearly defined and may not represent 95% CIs.) However, with the exception of the $\Phi = 1.3$ case, spectrally-estimated temperatures are lower than those reported by Meyer.

The left panel of Fig. 8 presents the spectrally-estimated temperature profiles for all pixels with a sufficient signal-to-noise ratio at heights of 5 mm, 10 mm, 20 mm and 40 mm above the burner for the $\Phi = 0.9$ flame. Error bars are not displayed to improve visualization, but errors are nominally $\pm 1\%$. The temperature profiles at heights of 5 mm and 10 mm are flat and rapidly decay within the thin mixing layer near $v = \pm 12.5$ mm. This nearly top-hat profile is consistent with the approximation of the flame as a single, homogeneous layer. However, at $u = 20$ mm, the mixing layer has widened slightly, and by $u = 40$ mm, the flame core only spans $|v| \leq 4$ mm. The right panel of Fig. 8 compares spectrally-retrieved temperature of the $\Phi = 0.9$ flame traversing vertically through the centerline ($v = 0$) with Meyer's OH absorption results [12]. Temperature increases rapidly above the base of the flame and peaks near 10 mm. The spectrally-estimated results are in good agreement with the laser measurements at each height investigated in Meyer's work.

The variation in scalar values with distance from the burner is presented for all equivalence ratios in Fig. 9. The results should be interpreted as path-averaged scalar values to recognize the significance of temperature and concentration gradients along the line-of-sight which become more prominent with increasing height. The cooler, outer edge of the flame contributes less to the path-integrated signal, so path-averaged temperatures will be lower than the center flame temperature. Additionally, the increasing size of the mixing layer makes it difficult to estimate absolute concentrations, so column densities are reported instead. The current two-dimensional path-averaged results are valuable for qualitative understanding of the flame. However, quantitative interpretation at heights $u > 10$ mm is not recommended since the impact of the mixing layer—which widens with height—is not accounted for. Retrieving three-dimensional scalar fields using a deconvolution technique is the ultimate goal of this effort.

Of particular interest is the variation in scalar values with equivalence ratio. All scalar values immediately increase with u. At each equivalence ratio, temperature, $q_{H_2O}(u)$, and $q_{CO_2}(u)$ rapidly increase and peak between $9\,\text{mm} \leq u \leq 12\,\text{mm}$. The initial behavior of $q_{CO}(u)$ is similar, but it reaches a maximum between $2\,\text{mm} \leq u \leq 4\,\text{mm}$. After reaching their peak values, the scalar quantities exhibit a gradual decay with u in a manner that is highly dependent on Φ. In the fuel lean flames ($\Phi = 0.8, 0.9$), the oxygen rich environment enables quick conversion

#216591 - $15.00 USD Received 9 Jul 2014; revised 15 Aug 2014; accepted 15 Aug 2014; published 29 Aug 2014

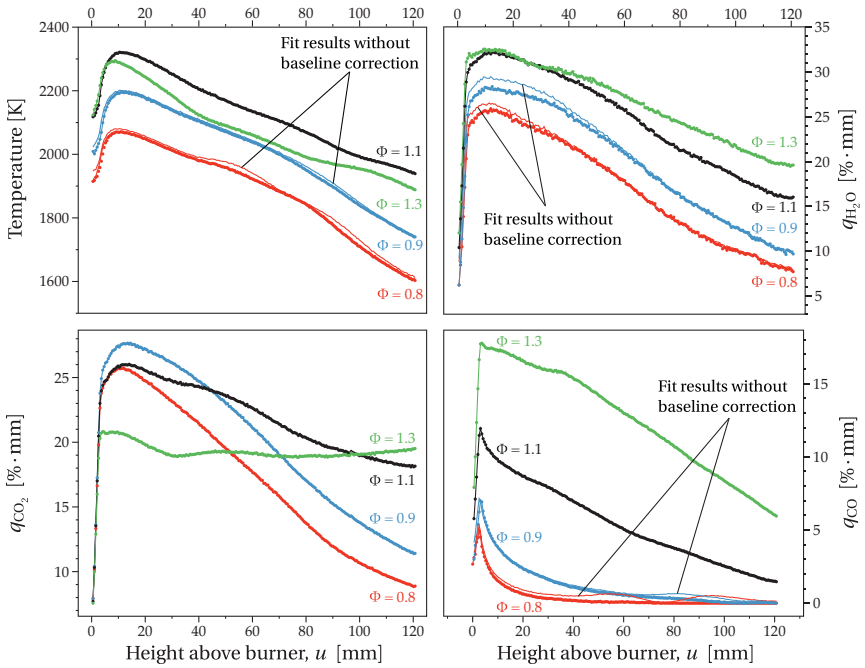

Fig. 9. Spectrally-retrieved scalar values of the C_2H_2/air flame, along the centerline ($v = 0$), for $\Phi = 0.8$ (● red), $\Phi = 0.9$ (● blue), $\Phi = 1.1$ (● black), and $\Phi = 1.3$ (● green). Error bars are omitted for clarity. Fit results obtained without the polynomial baseline correction for $\Phi = 0.8$ (— red) and $\Phi = 0.9$ (— blue) are annotated.

of CO to CO_2, and the CO_2 profiles follow an axial profile similar to H_2O. In the fuel rich flames ($\Phi = 1.1, 1.3$), the oxygen lean environment results in much larger CO concentrations near the burner and a more gradual conversion of CO to CO_2. While the N_2 co-flow limits diffusion of surrounding air into the flame, above $u = 30$ mm, the buoyancy forces lead to flame unsteadiness, and the entrainment of atmospheric O_2 is likely. (Recall the CoV map in Fig. 3.) It is reasonable that this increases the rate of CO $\rightarrow$ CO_2 conversion, as evidenced by a slight increase in slope of the $q_{CO_2}(u)$ curve for $\Phi = 1.1$ and a substantial increase in slope for $\Phi = 1.3$. The enhanced oxidation of CO at this height may be responsible for the observable change in the corresponding $T(u)$ curve. Between $10\,\text{mm} \leq u \leq 30\,\text{mm}$, the $T(u)$ slope is -3.9 K/mm and -5.5 K/mm for $\Phi = 1.1$ and $\Phi = 1.3$, respectively. Between $40\,\text{mm} \leq u \leq 70\,\text{mm}$, the slopes increase to -3.4 K/mm and -3.3 K/mm for $\Phi = 1.1$ and $\Phi = 1.3$, respectively.

As mentioned briefly before, spectra between $40\,\text{mm} \leq u \leq 90\,\text{mm}$ for $\Phi = 0.8$, and to a lesser extent for $\Phi = 0.9$, exhibit a subtle, low-frequency baseline oscillation. This oscillation produced a small bias in the T and q_{CO} fit parameters, and prompted the pragmatic addition of the 4$^{\text{th}}$-order polynomial to the model for the fuel-lean flames. This was the minimum order needed to visually account for the baseline oscillation; however, polynomials up to 7$^{\text{th}}$-order did not significantly affect the fit results. The baseline oscillation is a small fraction of the total signal and the polynomial never represented more than 1.5% of the peak spectral radiance. The baseline oscillation is likely a result of insufficient averaging over the intensity fluctuations arising from unsteady behavior in this flame region. It was not perceptible in the fuel-rich cases, and this is consistent with the smaller CoV values at $v = 0$ observed in Fig. 3. For comparison, the fit results obtained without using the 4$^{\text{th}}$-order polynomial to model the baseline are provided in Fig. 9 for context. The difference in $q_{CO_2}(u)$ is imperceptible. While the baseline

#216591 - $15.00 USD Received 9 Jul 2014; revised 15 Aug 2014; accepted 15 Aug 2014; published 29 Aug 2014

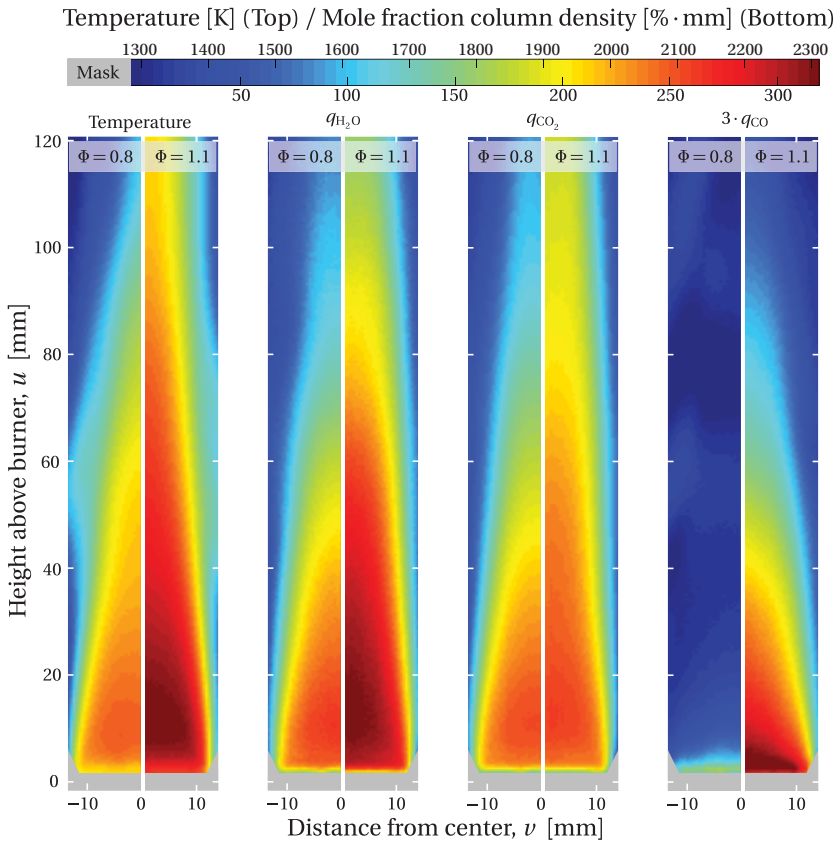

Fig. 10. Split imagery comparison of path-averaged scalar values for $\Phi = 0.8$ (left) and $\Phi = 1.1$ (right). *Left panel*: Temperature. *Center-left panel*: H_2O column density. *Center-right panel*: CO_2 column density. *Right*: Scaled CO column density. CO values are tripled to use the full range of the common color axis. The top and bottom color bar scales represent temperature and column density, respectively.

polynomial removes anomalous behavior in $q_{CO}(u)$ and $T(u)$ within the unsteady region, it also systematically lowers the $q_{H_2O}(u)$ column density where the flame is highly stable ($u < 40$ mm).

4.2.3. Scalar maps

Figure 10 compares two-dimensional (2-D) maps of temperature and column densities obtained from the $\Phi = 0.8$ and $\Phi = 1.1$ flames. These maps represent the most complete, spatially resolved, line-of-sight scalar value measurements of Hencken burner ethylene flames to date, and demonstrate the utility of IFTS for combustion diagnostics. The 2-D scalar profiles reveal the differences in combustion under fuel-lean and fuel-rich conditions. Most notable is the rapid conversion of CO to CO_2 in the $\Phi = 0.8$ flame, because of the abundance of available oxygen. This quick conversion of CO yields near identical H_2O and CO_2 maps in the $\Phi = 0.8$ flame. The $\Phi = 1.1$ flame has a large concentration of CO near the base. Diffusion and entrainment of surrounding air enables the gradual conversion of CO to CO_2, and the corresponding exothermicity of this reaction reduces the rate at which the path-averaged temperature decays with height, u.

#216591 - $15.00 USD Received 9 Jul 2014; revised 15 Aug 2014; accepted 15 Aug 2014; published 29 Aug 2014

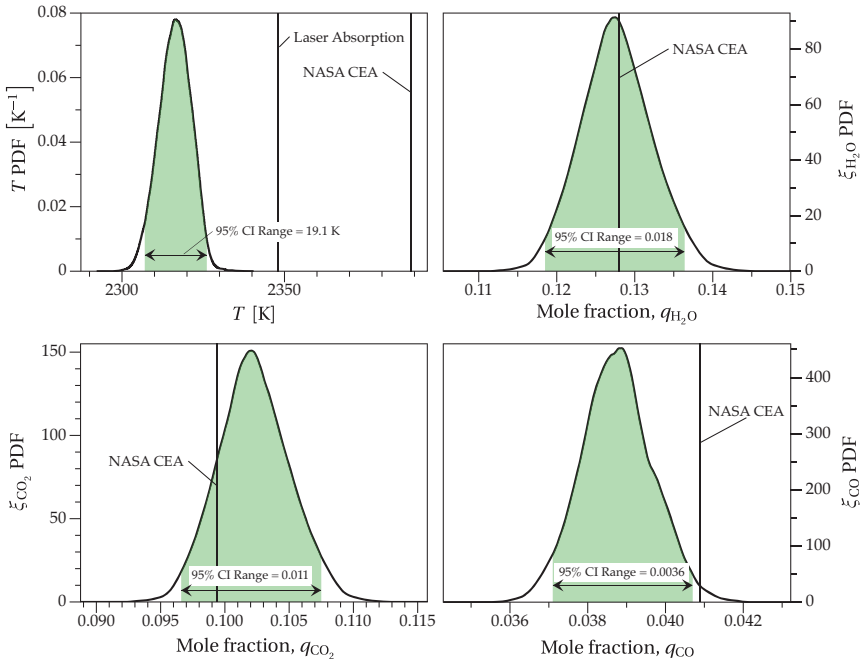

Fig. 11. Uncertainty distributions estimated from a 2,000 iteration Monte Carlo analysis to propagate calibration source uncertainties to the spectrally-retrieved scalar values. The shaded areas are centered at the mean value and correspond to the 95% confidence interval. Previous experimental and equilibrium results are provided for context.

4.3. Uncertainty estimation

An important source of systematic error in the spectrum, and consequently the estimation in scalar values, arises from imperfections in the calibration blackbody sources. High-temperature, wide-area blackbodies are necessary for calibrating flame measurements, but these are not as accurate as smaller blackbodies designed for calibrating lower temperature scenes. To assess the impact of absolute temperature and spectral emissivity uncertainty on the spectrally-retrieved scalar values, a Monte Carlo error analysis was performed. The manufacturer-specified 95% CIs for set-point temperatures and emissivities defined normal distributions from which random values were drawn. 2,000 iterations were performed, each time calibrating using blackbody temperatures and emissivities drawn from their respective uncertainty distributions. With each iteration, the spectral fits were performed leading to a distribution of scalar values which capture the uncertainty due to calibration. In general, these systematic calibration errors (δ_{cal}) were larger than the statistical uncertainty determined from the non-linear regression (δ_{nlr}). In this work, scalar value uncertainties represent the root quadrature sum of these two sources, i.e. $\delta_{\text{total}} = \sqrt{\delta_{\text{nlr}}^2 + \delta_{\text{cal}}^2}$.

The uncertainty distributions of T, ξ_{H_2O}, ξ_{CO_2} and ξ_{CO} obtained from the Monte Carlo error analysis of the $\Phi = 1.1$ flame spectrum at $(u, v) = (10\,\text{mm}, 0\,\text{mm})$ are presented in Fig. 11. Continuous probability distribution functions were estimated via kernel density estimation using the Epanechnikov kernel. The 95% CI for temperature spans 2307 K to 2326 K, which is more than 5 times larger than the regression uncertainty of 3.5 K. Adding in quadrature both the statistical fit error and the calibration systematic error yields a spectrally-estimated temperature of $T = (2318 \pm 19)$ K. Calibration errors had a much larger impact on the uncertainty of concen-

#216591 - $15.00 USD Received 9 Jul 2014; revised 15 Aug 2014; accepted 15 Aug 2014; published 29 Aug 2014

trations. For example, the H_2O mole fraction 95% CI (11.85 % to 13.64 %) is 15 times larger than the statistical fit uncertainty (0.12 %). Quadrature addition yields $\xi_{H_2O} = (12.6 \pm 0.8)\,\%$. The impact on the other flame species was similar and is reported in Fig. 11. Uncertainties of a few percent in blackbody temperature and emissivity affect the absolute radiometric accuracy much more than the relative spectral shape. Since the spectrally-retrieved temperature is strongly influenced by the relative line heights, whereas the column densities are dominated by the absolute line heights, the relative errors in temperature are much smaller than relative errors in column density.

5. Conclusions

This investigation of an ethylene flame ($\Phi = 0.8 - 1.3$) sought to establish IFTS as a useful combustion diagnostic. Spectrally-determined temperatures at all Φ values agree with previous laser absorption flame measurements of a similarly-configured Hencken burner. The large number of ro-vibrational emission lines and band structures arising from multiple species lead to statistical temperature uncertainties less than 50 K in the homogeneous flame region. Additionally, the retrieved H_2O, CO_2 and CO mole fractions are in excellent agreement with equilibrium predictions. The 2-D scalar fields obtained enable both the visualization and quantitative comparison of the Φ-dependent chemistry throughout the flame.

IFTS offers several unique advantages for combustion diagnostics. First, it is portable and can be set up and collecting calibrated spectral imagery in about an hour. Second, it enables the measurement of a moderate resolution spectrum (up to $0.25\,cm^{-1}$) across a wide band pass (1.5 µm to 5.5 µm). This represents highly constraining data which can be used to benchmark computational fluid dynamics simulations. As demonstrated, the spectra are readily interpreted in terms of 2-D path-averaged temperature and column density maps. Moreover, the adaptation of existing deconvolution algorithms to the high-fidelity hyperspectral flame images may enable the retrieval of the 3-D scalar fields. The high-speed imagery existing within the interferometric measurement enables visualization of flame dynamics, and this enhances interpretation of 2-D scalar fields derived from the time-averaged spectra. Additionally, existing flow field analyses currently performed by infrared cameras can be readily adapted to the broadband imagery captured within the IFTS measurement. However, as a passive measurement, IFTS does not have the same sensitivity to trace species that lasers enjoy, and homonuclear diatomic molecules (e.g. H_2) cannot be observed. Additionally, the slow speed (0.1 Hz to 10 Hz) at which typical IFTS measurements are captured requires statistically significant numbers of observations (100–1000) to properly average over temporal fluctuations in the scalar fields.

#216591 - $15.00 USD Received 9 Jul 2014; revised 15 Aug 2014; accepted 15 Aug 2014; published 29 Aug 2014